Manuscript submitted to **Biophysical** *Journal*
Article

Strain stiffening of the Ndc80 complex

Felix Schwietert[1], Vladimir A. Volkov[2,3], Pim J. Huis in 't Veld[4], Marileen Dogterom[3], Andrea Musacchio[4], and Jan Kierfeld[1,*]

[1]Physics Department, TU Dortmund University, Dortmund, Germany
[2]School of Biological and Behavioural Sciences, Queen Mary University of London, London, UK
[3]Department of Bionanoscience, Faculty of Applied Sciences, Delft University of Technology, Delft, Netherlands
[4]Department of Mechanistic Cell Biology, Max Planck Institute of Molecular Physiology, Dortmund, Germany
[*]Correspondence: jan.kierfeld@tu-dortmund.de

ABSTRACT

In the mitotic spindle, microtubules attach to chromosomes via kinetochores. The microtubule-binding Ndc80 complex is an integral part of kinetochores, and is essential for kinetochores to attach to microtubules and to transmit forces from dynamic microtubule ends to the chromosomes. The Ndc80 complex has a rod-like appearance with globular domains at its ends that are separated by a long coiled coil. Its mechanical properties are considered important for the dynamic interaction between kinetochores and microtubules. Here, we present a novel method that allows us to time-trace the effective stiffness of Ndc80 complexes following shortening microtubule ends against applied force in optical trap experiments. Applying this method to wild type Ndc80 and three variants (CH-domains mutated or Hec1-tail unphosphorylated, phosphorylated, or truncated), we reveal that each variant exhibits strain stiffening, i.e., the effective stiffness increases under tension that is built up by a depolymerizing microtubule. The strain stiffening relation is roughly linear and independent of the state of the microtubule. We introduce a polymer model for the Ndc80 complex, which shows that the strain stiffening can be traced back to the specific architecture of the Ndc80 complex with a characteristic flexible kink and the bending elasticity of flaring protofilaments, which exert force to move Ndc80 complexes. Our model accounts for changes in the amount of load-bearing attachments at various force levels and reproduces the roughly linear strain stiffening behavior, highlighting the importance of force-dependent binding affinity.

SIGNIFICANCE

By time-tracing the stiffness of microtubule end-tracking Ndc80 complexes in optical trap experiments, we detect strain stiffening, and, thereby, provide new insights into the elastic properties of the Ndc80 complex. The strain stiffening is robust against mutations in the Ndc80 complex. We relate strain stiffening to the structure of the Ndc80 complex by means of a simple polymer model, and to the flexibility of force-generating flaring protofilaments at the tip of the microtubule. Since Ndc80 complexes play a major role for transmitting force from microtubule ends to the kinetochore, their elastic properties are of great interest for a deeper understanding of chromosome dynamics in the mitotic spindle.

INTRODUCTION

In the mitotic spindle, microtubules (MTs) attach to chromosomes via macromolecular structures called kinetochores (1). Kinetochores bind to MTs via attachments created by Ndc80 complexes (2). The Ndc80-mediated attachments remain intact while dynamic MTs alternate between growth and shrinkage, and transmit depolymerization forces to the kinetochore during the segregation of chromosomes. The exact mechanisms underlying binding and force transmission are not completely understood but are expected to reflect the molecular structure and resulting elastic properties of the Ndc80 complex.

The Ndc80 complex is a 4-subunit rod-like coiled-coil with a characteristic flexible kink at approximately one third of its length (3, 4). MT binding is performed by the globular calponin homology (CH) domains near the N-terminal ends of the Ndc80 and Nuf2 subunits, and an unstructured N-terminal tail. In vitro experiments reveal that a single Ndc80 complex is not able to track dynamic MT ends (5–7), whereas tracking activity is attained by multimerization (5, 7) and in presence of Dam1 or Ska complexes (6, 8, 9). Moreover, an unstructured positively charged Ndc80 tail that precedes the CH domain is crucial for

MT tip tracking (10), and phosphorylation of the tail or introduction of negative charges reduces the binding affinity of the Ndc80 complex to the MT lattice (2, 11–14).

Early theoretical models of spindle-kinetochore dynamics envisioned a static Hill sleeve with rigid linkers (15, 16) or motor proteins mediating MT–kinetochore attachment and movement (17). More recent studies included (visco)elastic MT–kinetochore linkers with a constant stiffness, which had to be estimated (18–21). One such model identified the linker stiffness as a critical parameter for the occurrence of chromosome oscillations during metaphase (22). With the identification of the Ndc80 complex as the crucial linker, understanding its elastic properties has now become crucially important to dissect how MT depolymerization forces are transmitted to the kinetochore to generate movement. The elastic properties of the Ndc80 complex in its MT-bound state, in particular its stiffness under tension, are the main subject of this work.

Measurements of stiffness can confirm structural models if they are in agreement with elastic models derived from the available structural information on the Ndc80 complex. The elastic properties of the Ndc80 complex were studied experimentally by optical trapping methods introduced in Ref. (7). Here, we re-analyzed them using novel theoretical analysis and modeling approaches. In those experiments, the stiffness of Ndc80 complexes was found to increase under tension (7). Whereas in those experiments the stiffness was only determined while the Ndc80 complexes were attached to a stalled MT, here, we re-evaluate the same data with a novel method that allows us to time-trace the stiffness, i.e., to determine the stiffness of Ndc80 complexes while it tracks a polymerizing or depolymerizing MT against the opposing load from the optical trap. By splitting the force traces into fixed time intervals, and analyzing stiffness at each of them, we achieve several advantages: (1) we generate more data over a wider force range; (2) we demonstrate stiffening during force production and not only compare stalled MTs to free ones; (3) we alleviate the concern that different levels of strain stiffening result from differences in MT ends or beads. Time-tracing also allows us to establish that strain stiffening does not depend on the the state of the MT end: we observe positive correlation of stiffness with force when the MT stalls, grows, or shrinks. In addition to wild type Ndc80, we also analyze data from MT end-tracking experiments with Ndc80 complexes whose tails are phosphorylated or truncated (10), or harboring CH domains that are mutated to greatly reduce MT binding. We observe strain stiffening for each of those Ndc80 mutations and draw conclusions on the role of the tail domain in MT binding.

In order to rationalize the experimental findings on strain stiffening of the Ndc80 links, we introduce a simple polymer model for the Ndc80 complex. Describing Ndc80 as an ideal chain with two bonds of different lengths, we show that the strain stiffening is a direct consequence of the characteristic Ndc80 structure with its two stiff rods that are connected flexibly. To match the measured stiffnesses it is necessary to include the contribution from protofilament (PF) bending to the total effective stiffness. Finally, to explain the shape of the experimental force–stiffness relations also introduce a positive correlation of the number of MT end-attached Ndc80 complexes with MT-generated force.

MATERIALS AND METHODS

Experimental methods

Cloning and purification

The Ndc80 CH-mutant contains Hec1 K89A, Hec1 K166A, Nuf2 K41A, and Nuf2 K115A: four mutations that reduce the binding of Ndc80 to microtubules (23). Mutations were introduced into pLIB-Hec1 and pLIB-Nuf2 vectors using site-directed mutagenesis and Gibson assembly. Expression cassettes containing mutated Hec1, mutated Nuf2, Spc25-Sortase-Hexahistide and Spc24-Spy were combined on a pBIG1 plasmid and integrated into a single baculovirus for expression in insect cells (24). The Ndc80 CH-mutant was purified and linked to T_1S_3 modules (25) as previously described in detail for wild-type, tailless, and phosphorylated Ndc80 variants (7, 10).

Optical trap experiments

Optical trap experiments with dynamic MTs and Ndc80 were performed as described previously (7, 10). In brief, 1 µm silica beads were coated with poly-L-lysine-grafted polyethyleneglycole (PLL-PEG) as described previously (7). 1–10 % of the PLL-PEG carried a biotin, and was subsequently saturated with $T_1S_3[\mathrm{Ndc80}]_3$ modules. Ndc80-TMR fluorescence on the bead was measured to determine the coating density, and bead preparations containing on average 100–1000 Ndc80 copies per bead were used for optical trapping.

The microscopic flow-chambers were assembled using glass slides and coverslips treated with 2 % dichlorodimethylsilane. The chambers were incubated with 0.2 µM of anti-digoxigenin IgG (Roche). Non-specific binding of molecules to coverslips was prevented by an incubation with 1 % Pluronic F-127. Then, GMPCPP-stabilized, digoxigenin-labeled MT seeds were attached to the coverslips. Finally, $T_1S_3[\mathrm{Ndc80}]_3$-coated beads were introduced in a reaction mix containing 10–12 µM tubulin, 1 mM GTP, 1 mg/ml κ-casein, 4 mM DTT, 0.2 mg/ml catalase, 0.4 mg/ml glucose oxidase and 20 mM glucose.

Optical trapping experiments were performed as described previously (7). Before each experiment, a free bead was

attached to a MT near its growing end and held in an optical trap with a stiffness of 0.02–0.04 $\mathrm{pN\,nm^{-1}}$. Position of the bead was continuously recorded at 10 kHz using a quadrant detector, and differential interference contrast (DIC) images were simultaneously recorded to monitor positions of the bead and the dynamics of MTs. The bead was held in a trap until the MT depolymerized, which resulted in two alternative outcomes: the bead–MT connection broke, or the bead rescued the MT shortening, and the MT started regrowing. In case of a rescue, recordings were stopped arbitrarily after 30 or more minutes by increasing the trap stiffness to 0.2–0.4 $\mathrm{pN\,nm^{-1}}$ and rupturing the bead–MT connection. Quadrant detector readings of the bead position were later turned so that one of the axes corresponded to bead displacement along MT to generate time traces $x(t)$ of the bead position.

Time-tracing the stiffness

As long as the mean bead position is stationary, e.g. during MT stall, the effective stiffness can be easily calculated from the variance of the bead position x by $k_\mathrm{B}T/\mathrm{Var}(x)$. We now present a method that enables us to monitor the stiffness over time, i.e., also during polymerization and depolymerization phases of the MT, and to observe strain stiffening of the Ndc80 complex in the course of a single experiment. We divide the signal into several intervals k of a certain length for each of which we will determine a stiffness as sketched in Fig. 1. For that purpose, we do not use the variance over that interval but the mean squared distance from a quasi-equilibrium bead position which may slowly vary over time. We estimate the time course of the quasi-equilibrium bead position with a linear fit $f_k(t)$ to the entire time trace $x_k(t)$ in an interval k. Then, the effective stiffness during the interval k is given by the inverse of the mean squared distance

$$c_k = \frac{k_\mathrm{B}T}{\langle (x_k(t) - f_k(t))^2 \rangle}. \tag{1}$$

Finally, we can assign a force F_k on the Ndc80 link to each interval, which can be calculated from the trap stiffness and the mean bead position during that interval, $F_k = c_\mathrm{trap}\langle x_k \rangle$.

Theoretical Model

Before modeling the outcomes of the stiffness measurements, we have to identify the elastic elements that contribute to the total stiffness as sketched in Fig. 2B. The stiffness of the optical trap will always be present in the measurements. Its value is determined during the calibration of the optical trap after the bead detached from the MT.

What we are interested in, is the stiffness of the entire Ndc80–MT link. Within this entity, we identify three potentially elastic elements: First, the Ndc80 complex can act as an entropic spring with stiffness c_Ndc due to its flexible kink. Secondly, the bond between the Ndc80 trimer and the MT may exhibit some effective elasticity c_bond, e.g. as a consequence of unbinding and rebinding of individual Ndc80 units. Finally, stretching the flaring ends of the PFs at the MT tip out of their preferred curvature may produce an effective stiffness c_PF for pulling in the axial direction of the MT. Outside the Ndc80–MT link, the PLL-PEG that connects the Ndc80 complexes with the bead should be taken into account as another elastic element between the bead and the MT, generating a fourth stiffness c_PEG.

Each of the four stiffnesses may depend on the applied force and exhibit strain stiffening itself. Since the three elements are aligned in series, their inverse stiffnesses sum up to the inverse stiffness $\tilde{c}^{-1}$ of a Ndc80 complex that is attached to a PF:

$$\tilde{c}(F) = \left(\frac{1}{c_\mathrm{PEG}(F)} + \frac{1}{c_\mathrm{Ndc}(F)} + \frac{1}{c_\mathrm{bond}(F)} + \frac{1}{c_\mathrm{PF}(F)} \right)^{-1}. \tag{2}$$

It is important to note that this reduces the total stiffness and that the softest elastic element dominates the total stiffness.

It is possible that multiple Ndc80 complexes are attached parallelly to the MT. For the sake of simplicity, we will always assume that each PF can only attach one Ndc80 complex and that the parallel PFs and Ndc80 complexes have the same elongation, respectively. Then, the force F is shared equally between the parallel Ndc80–PF units with stiffness $\tilde{c}(F)$, so that the resultant stiffness of n parallelly attached Ndc80 complexes can be written as

$$\tilde{c}_n = n\,\tilde{c}\left(\frac{F}{n}\right). \tag{3}$$

Although parallel stiffnesses add up, the shared force can give rise to an overall reduction $\tilde{c}_n(F) < \tilde{c}(F)$ of the cooperative stiffness if the individual stiffness exhibits strain stiffening $c(F) \propto F^m$ with an exponent $m > 1$. We will find below that such strain stiffening behavior is realized both for Ndc80 and PF stiffness.

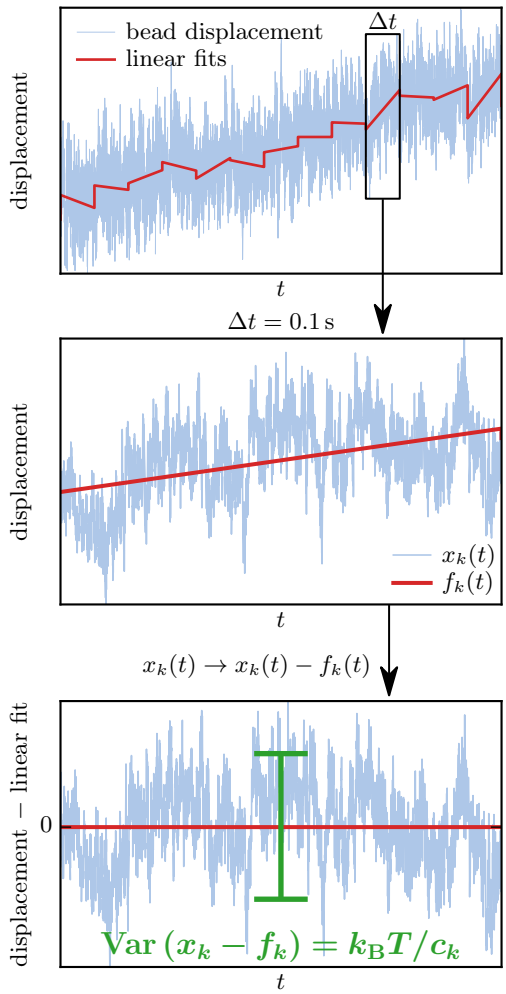

Figure 1: Stiffness time-tracing. The signal is divided in intervals of 0.1 s, which gives 1000 data points per interval at a sampling rate of 10 kHz. For each interval, we estimate the evolution of the equilibrium bead position with a linear fit $f_k(t)$. The stiffness of an interval is then given by Eq. 1, where the variance equals the mean squared distance of the bead position $x_k(t)$ from the estimated equilibrium $f_k(t)$.

Bond stiffness

The bond between individual Ndc80 complexes and the MT is established by the globular regions at the N-terminal of the complex (3, 23, 26) via calponin-homology (CH) domains (27). Also the N-terminal tail of the Ndc80 subunit could be involved in MT binding (1, 28). The effective stiffness of the Ndc80–MT bond is hard to model because the exact binding mechanism to the MT is still elusive. Because the Ndc80 CH domain and the N-terminal tail are relevant for binding to the MT, investigation of the stiffness changes for mutants Ndc80$^{\Delta 80}$ and Ndc80^{CHmut} as compared to the wild type Ndc80^{wt} will allow us to address this issue in the Discussion section. We will first concentrate on the contributions of the Ndc80 complex itself, the PF and the PLL-PEG in the following.

Ndc80 stiffness

In order to model the stiffness of the Ndc80 complex under force, we use a simple polymer model that is based on the known structure (3, 4): The Ndc80 complex is a tetramer with a total length of 56 nm and consists of two stiff arms with lengths $a = 40\,\mathrm{nm}$ and $b = 16\,\mathrm{nm}$, see Fig. 2C. In the cell, the long arm is bound to the kinetochore, in the experiment it is bound to the glass bead, while the short arm can attach to a MT. We describe the conformation of the two arms by two vectors $\vec{a}$ and $\vec{b}$ in

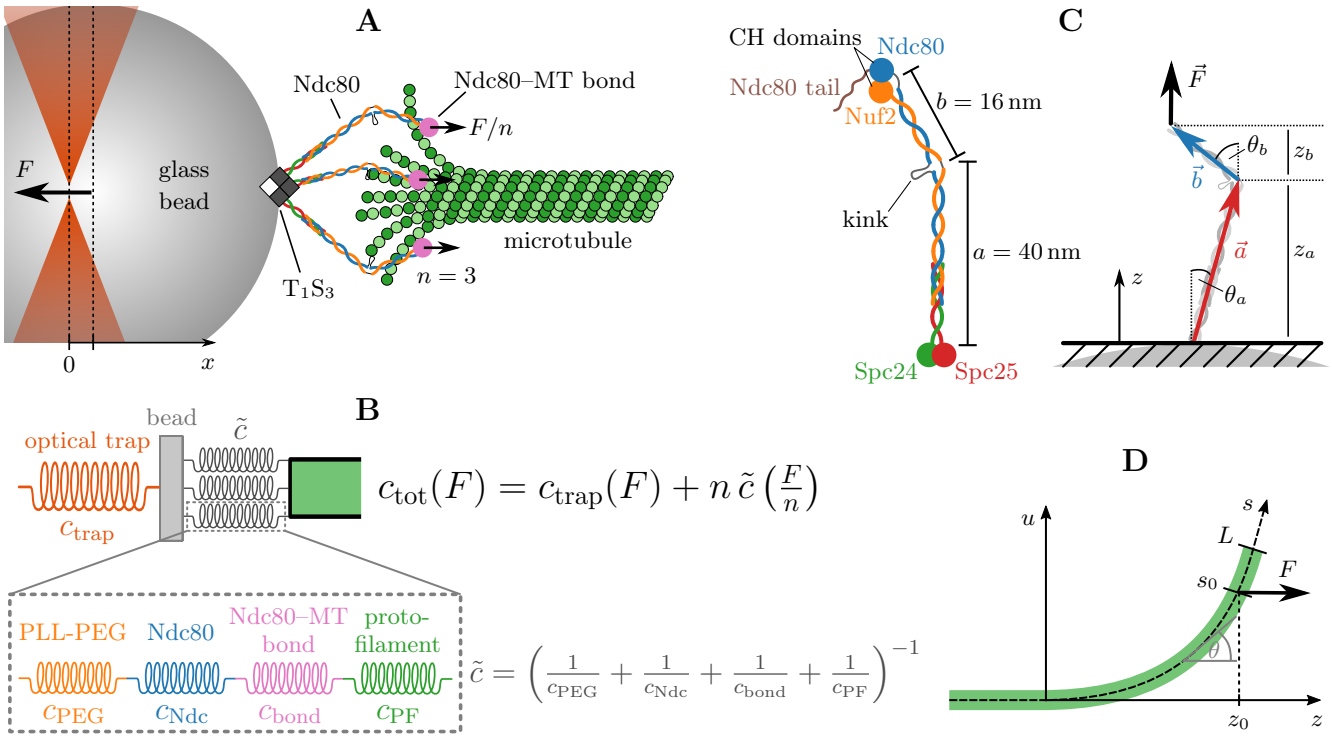

Figure 2: (A) Sketch of the experiment (not true to scale) with $n = 3$ attached Ndc80 complexes. We assume that each Ndc80 complex is exposed to the same force F/n. (B) Spring model. Between the bead and the MT, there are four potentially elastic objects, which are aligned in series: the PLL-PEG, the Ndc80 complex, the Ndc80–MT bond and the curved PF. When n Ndc80 complexes are attached to the MT, n of those serial combinations act as parallel springs. (C) Ndc80 complex as FJC. The Ndc80 complex is a tetramer with a total length of 56 nm and a flexible kink at 40 nm. The long arm a is bound to the glass bead, the short arm b to the MT. We model the Ndc80 complex as a FJC with two bonds $\vec{a}$ and $\vec{b}$, which have the different lengths a and b. (D) Model for PF bending. The z-axis marks the direction along the MT, s is the position along the curved PF. The Ndc80 complex is attached at $s = s_0$ and applies the force F in z-direction.

polar coordinates as shown in Fig. 2C:

$$\vec{a} = a \begin{pmatrix} \sin\theta_a \cos\varphi_a \\ \sin\theta_a \sin\varphi_a \\ \cos\theta_a \end{pmatrix}, \quad \vec{b} = b \begin{pmatrix} \sin\theta_b \cos\varphi_b \\ \sin\theta_b \sin\varphi_b \\ \cos\theta_b \end{pmatrix}. \tag{4}$$

The impenetrable glass bead restricts these two vectors in the experiment. Since the diameter of the glass bead (1 µm) is much larger than the Ndc80 complex we approximate the bead as a plain surface that confines the Ndc80 complex to the upper half space, so that $z_a > 0$ and $z = z_a + z_b > 0$, see Fig. 2C. Experiments have shown that the two arms are connected flexibly within an angular range between 0° ($\vec{a}$ and $\vec{b}$ in line) and 120° (maximally kinked) (4). Since we want to model the Ndc80 complex while it is confined by the glass bead and under the influence of an external stretching force that is applied in z-direction and favors small angles, we can neglect the constraint to angles below 120°. This allows us to perform an explicit analytical calculation, as we reduce the Ndc80 complex to a purely entropic freely jointed chain (FJC) with two bonds of different lengths. The only energy is the stretching energy from a constant external force $\vec{F} = F\vec{e}_z$ in positive z-direction,

$$E_{\mathrm{FJC}} = -\vec{F} \cdot (\vec{a} + \vec{b}) = -F(z_a + z_b) = -F(a\cos\theta_a + b\cos\theta_b). \tag{5}$$

Respecting the confinement to the upper half-space we obtain the canonical partition function ($\beta \equiv 1/k_{\mathrm{B}}T$):

$$Z(F) = \iint\limits_{z_a, z > 0} \mathrm{d}\theta_a \sin\theta_a \mathrm{d}\theta_b \sin\theta_b \, \mathrm{e}^{-\beta E_{\mathrm{FJC}}}. \tag{6}$$

Both the extension–force relation $z(F)$ and the stiffness–force relation $c_{\mathrm{Ndc}}(F)$ in the presence of thermal fluctuations can be obtained from derivatives of the partition function with respect to the force:

$$z(F) = \langle z \rangle = \frac{1}{\beta}\partial_F \ln Z, \quad c_{\mathrm{Ndc}}(F) = \left(\frac{\partial z(F)}{\partial F}\right)^{-1} \tag{7}$$

The explicit result for the stiffness of the Ndc80 complex is

$$\begin{aligned} c_{\mathrm{Ndc}}(F) = \Bigg[& \frac{2}{\beta F^2} + \beta \frac{2\mathrm{e}^{\beta F a}\left((a^2+b^2)\sinh\beta F b + 2ab\cosh\beta F b\right) - b^2 \mathrm{e}^{\beta F b}}{2\mathrm{e}^{\beta F a}\sinh\beta F b - \mathrm{e}^{\beta F b} - \beta F b + 1} \\ & - \beta \left(\frac{2\mathrm{e}^{\beta F a}(a\sinh\beta F b + b\cosh\beta F b) - b\mathrm{e}^{\beta F b} - b}{2\mathrm{e}^{\beta F a}\sinh\beta F b - \mathrm{e}^{\beta F b} - \beta F b + 1} \right)^2 \Bigg]^{-1}. \end{aligned} \tag{8}$$

In the limit of strong forces, this simplifies to

$$z(F) = a + b - \frac{2}{\beta F}, \quad c_{\mathrm{Ndc}} = \frac{\beta F^2}{2}, \tag{9}$$

which is a general result for arbitrary FJC polymer models under force, where the relative extension of a FJC of total length L and bond length b saturates according to $1 - z(F)/L \propto k_B T/bF$ (29, 30).

Protofilament stiffness

We assign a stiffness to the PF by modeling it as a beam with a preferred curvature ϕ and persistence length L_{p}. As described in Fig. 2D, the PF is straight and bound by lateral interactions with neighboring PFs for $z < 0$. For $z > 0$, we assume that there are no interactions to neighboring PFs so that the PF can bend freely. The PF conformation is described by the local bending angle $\theta(s)$ at the position s along the PF. The PF curvature is obtained by the derivative $\dot{\theta}(s) = \mathrm{d}\theta/\mathrm{d}s$. In the absence of an external force, the PF has a preferred (or spontaneous) constant curvature ϕ. Let the Ndc80 complex attach at the position $s = s_0$ and apply a force F in z-direction. Then, the total energy is the sum of bending and stretching energies,

$$E_{\mathrm{PF}} = \int_0^L \left(\frac{\alpha}{2}\left(\dot{\theta} - \phi\right)^2 - zF\delta(s - s_0) \right) \mathrm{d}s, \tag{10}$$

with the bending stiffness $\alpha = k_{\mathrm{B}} T L_{\mathrm{p}}$ and the total length L of the free PF; the δ-function describes a point force applied at $s = s_0$. The PF is dominated by the interplay of bending and stretching energy such that we can neglect thermal fluctuations and obtain the PF stiffness from the configuration minimizing the total energy E_{PF}. Since the force F only affects the shape of the PF for $s < s_0$ while the curvature at $s > s_0$ stays ϕ, we have to minimize the PF energy with boundary conditions $\theta(0) = 0$ and $\dot{\theta}(s_0) = \phi$. The energy minimizing PF configuration satisfies the Euler-Lagrange equation $\ddot{\theta} = \frac{F}{\alpha}\sin\theta$, which we solve numerically with a shooting method in order to fulfill the boundary conditions. The effective deflection is given by the position of the point of force application on the z-axis $z_0 = z(s_0)$. Finally, the effective stretching stiffness of the PF can be determined from the derivative of the deflection:

$$z_0(F) = \int_0^{s_0} \cos\theta(s)\,\mathrm{d}s, \quad c_{\mathrm{PF}} = \left(\frac{\mathrm{d}z_0}{\mathrm{d}F}\right)^{-1}. \tag{11}$$

In the limit of strong forces, the PF is stretched, i.e., $\theta(s) \ll 1$, and we can approximate the differential equation by $\ddot{\theta} = (F/\alpha)\,\theta$, which can be solved analytically:

$$z_0(F) \approx s_0 \left(1 - \frac{\phi^2}{4s_0}\left(\frac{\alpha}{F}\right)^{3/2}\right), \qquad c_{\mathrm{PF}}(F) \approx \frac{8F^{5/2}}{3\phi^2 a^{3/2}} \propto F^{\frac{5}{2}}. \tag{12}$$

We note the pronounced strain stiffening with $c_{\mathrm{PF}}(F) \propto F^{5/2}$, which is a consequence of bending rigidity together with spontaneous curvature. The model depends on three parameters: The persistence length L_{p}, the preferred curvature ϕ, and the point of force application s_0. Following the results of in vitro experiments (31), we use $L_{\mathrm{p}} = 200\,\mathrm{nm}$ and $\phi = 20^\circ$ per dimer throughout the paper. We have to guess where the Ndc80 complex attaches to the PF. Since the attachment point has to be somewhere on the PF, s_0 has to be smaller than L, which is the length of the curved part of the PF. McIntosh *et al.* (31) measured values in the range of 10 to 80 nm for depolymerizing MTs in vitro. In this paper, we will use estimates $s_0 = 20\,\mathrm{nm}$ and $s_0 = 50\,\mathrm{nm}$.

PEG stiffness

We estimate the PEG stiffness on the basis of the extended FJC model for the elasticity of PEG provided by Oesterhelt *et al.* (32). Since PEG that is dissolved in water undergoes a conformational transition from a helical to a planar structure when tension is applied, the model includes two distinct bond lengths, one for each of the conformations. Assuming a Boltzmann distributed ratio of helical and planar monomers, the authors obtain an effective bond length that depends on the applied force. We derive the PEG stiffness c_{PEG} from the extension–force relation $L(F)$ that is given in Eq. 2 in Ref. (32):

$$c_{\mathrm{PEG}}(F) = \left(\frac{\mathrm{d}L(F)}{\mathrm{d}F}\right)^{-1}. \tag{13}$$

For the PEG-2000 used in our experiments, we evaluate the equations with a number of $N_{\mathrm{S}} = 45$ segments while keeping the other parameters as listed in Ref. (32) (see Supporting Material for more details).

RESULTS

Strain stiffening can be observed for several Ndc80 variants

The ability of different Ndc80 variants to track and stall depolymerizing MTs has been examined in two previous studies (7, 10). Here, we re-examined the underlying data to determine effective stiffnesses for wild type Ndc80 complexes ($\mathrm{Ndc80^{wt}}$) as well as three variants, including Ndc80 complexes with a phosphorylated tail ($\mathrm{Ndc80^{P}}$), Ndc80 complexes, whose tail has been truncated ($\mathrm{Ndc80^{\Delta 80}}$), and Ndc80 complexes with mutated CH domains and a greatly reduced MT binding ($\mathrm{Ndc80^{CHmut}}$).

In Ref. (7), the stiffnesses for the wild type Ndc80 were determined from the variance of bead positions during MT stall, which gave one stiffness per experiment. These experiments revealed stiffening under force. However, the stall force is related to the Ndc80 density on the bead and therefore probably also to the number of Ndc80 complexes that are attached to the MT. For this reason, we can not determine whether the stiffening is an intrinsic property of the Ndc80 complex and/or the PF, or whether it arises from a higher number of parallelly attached Ndc80 complexes.

To settle this issue, we need to time-trace the stiffness throughout a *single* experiment. We achieve this by binning the data of bead positions in intervals of 0.1 s and determining an effective stiffness and applied force for each interval separately using the procedure described in the Materials and Methods section. This allows us to determine the stiffness while the depolymerizing MT pulls the attached bead and thereby increases the force. In other words, we measure the stiffness for different forces in a single experiment and, thus, with a fixed Ndc80 density on the bead. The results of this analysis are shown in Fig. 3A-D for four representative examples for the four Ndc80 variants, as well as in Fig. S1 in the Supporting Material for twelve further examples.

For each of the Ndc80 variants, there are experiments in which we detect a smooth stiffening behavior when the tension increases, but there are also experiments that do not exhibit any stiffening at all as in Fig. 3D. Based on previously observed absence of stiffening during lateral bead–MT attachment (7), we interpreted experiments without stiffening as laterally attached and excluded them from the following analyses. Experiments with observed stiffening were interpreted as resulting from the end-on attachment that is sketched in Fig. 2A and analyzed further. Stiffening was observed in 32 of 53 experiments with $\mathrm{Ndc80^{wt}}$, 8/24 with $\mathrm{Ndc80^{\Delta 80}}$, 12/32 with $\mathrm{Ndc80^{CHmut}}$, and 14/29 with $\mathrm{Ndc80^{P}}$. Calibrations of QPD voltage to obtain bead displacement, as well as calibrations of trap stiffness as a function of bead's displacement from the trap center were linear within 200 nm from the trap center. Therefore, displacements of a bead from the trap center that exceeded 200 nm were excluded from the following analyses of the strain stiffening.

In the experiments that exhibit stiffening, the MT depolymerization typically stalls at some force for $\mathrm{Ndc80^{wt}}$ and $\mathrm{Ndc80^{P}}$, but not for $\mathrm{Ndc80^{\Delta 80}}$ and $\mathrm{Ndc80^{CHmut}}$, where the bead typically detaches before it can stall the MT, see Fig. 3B. This indicates that the detachment force for $\mathrm{Ndc80^{\Delta 80}}$ and $\mathrm{Ndc80^{CHmut}}$ is usually below the MT stall force under the experimental conditions applied. Therefore, a systematic analysis of these mutants is only enabled by time-tracing of the stiffness prior to detachment, as measurements in a stalled state are rarely possible. The decrease in detachment force also confirms that the combination of the tail and the CH domain is essential for force-resisting attachment (10).

A stall can be interrupted in two possible ways: Either the bead detaches from the MT (Fig. 3A), or MT growth is rescued (Fig. 3C). In the first case, the bead relaxes immediately to the equilibrium position of the optical trap and the measured stiffness is the trap stiffness c_{trap}. In case of a rescue, the bead stays attached to the polymerizing MT and the tension decreases until the MT undergoes a catastrophe and starts depolymerizing again. This will allow us to investigate stiffening of the Ndc80 complexes in dependence of the dynamic state of the MT in the following section.

Another advantage of our time-tracing method is that we generate many more data points from the same number of experiments. While, for example, 53 stiffnesses of $\mathrm{Ndc80^{wt}}$ were determined in Ref. (7) from stalling MTs, time-tracing generates 4403 stiffnesses from the same experiments (see Fig. S2 in the Supporting Material). The cumulated force–stiffness

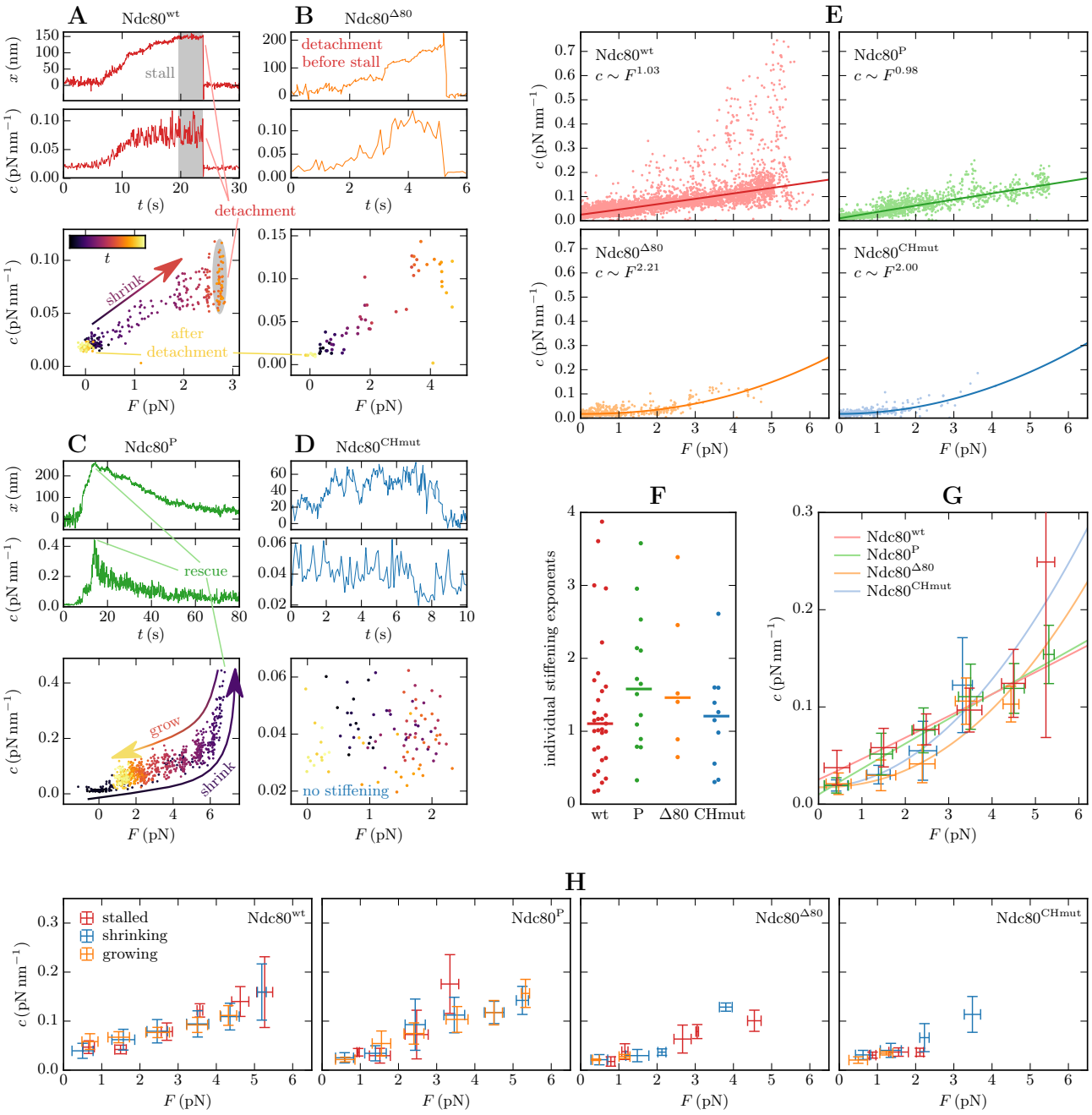

Figure 3: (A-D) Four representatives for typical behavior during single experiments. More examples are shown in Fig. S1 in the Supporting Material. For each experiment, the upper two plots show the piecewise linearized bead position and the stiffness over time, while the stiffness–force relation is depicted in the bottom plot, in which the time is represented by the color gradient. When the force is increased due to the shrinking MT, we can observe stiffening in most experiments (A-C). Shrinking usually is followed by a stall phase with constant force and constant stiffness (gray), except for experiments with Ndc80$^{\Delta 80}$ (B) and Ndc80^{CHmut}, in which the bead usually detaches before reaching the stall force. The stall is terminated either by detachment (A) or by MT rescue (C). After detachment the bead relaxes to $x = 0$ and we measure the trap stiffness. When the MT is rescued and grows, the stiffness–force relation traces the same curve as during depolymerization. (E) Robust power fits. For each Ndc80 variant, the combined stiffness data from all experiments (dots) is robustly fitted with power functions $c(F) = aF^m + c_0$ (lines) as described in the Supporting Material. The offset c_0 should respect the trap stiffness. (F) Stiffening exponents m that result from applying the power fits to those single experiments, where a proper stiffening is recognizable and the bead was attached to the MT for at least 1 s, so that there are $\geq$10 stiffnesses to fit to. The horizontal bars mark the medians. (G) Summarized stiffness–force relations for Ndc80^{wt}, Ndc80$^{\Delta 80}$, and Ndc80^{CHmut}. The error bars represent the standard deviation in F and in c of the points within each bin. The lines show the power fits from (E). (H) Stiffnesses separately evaluated for stalled, shrinking, and growing MTs.

data, which are collectively depicted in Fig 3E for each Ndc80 variant, reveal the strain stiffening more clearly than the sole use of the stalls in Ref. (7) and allow for a more thorough analysis and interpretation.

In order to further characterize strain stiffening, we fit power law functions $c(F) = aF^m + c_0$ to the collective data by use of a robust regression minimizing the Huber loss (33), see Fig. 3E and Supporting Material. The exponent m characterizes the observed strain stiffening behavior. We account for the trap stiffness by the offset c_0 for which the fits yield results that, indeed, lie in a range $0.01\,\mathrm{pN\,nm^{-1}}$ to $0.025\,\mathrm{pN\,nm^{-1}}$, which is in accordance with the trap stiffnesses determined during calibration. While the stiffnesses exhibit a linear dependence on force with exponents m around unity for Ndc80^{wt} and Ndc80^{P}, the stiffness–force relations of Ndc80$^{\Delta 80}$ and Ndc80^{CHmut} have a roughly parabolic shape ($m \approx 2$). We note that for Ndc80$^{\Delta 80}$ and Ndc80^{CHmut}, there are few data for high forces, making the stiffening exponents less reliable.

The stiffening exponents determined in Fig. 3E are the result of a fit to the combined data from several experiments, and may be biased by the correlation between the stall force and the Ndc80 densities on the bead. Our new time-tracing analysis, however, dampens this bias compared to the sole analysis of the stalls as stiffnesses are determined for small forces but at high Ndc80 densities during MT depolymerization in the respective experiments. We also apply the power law regressions to the stiffness–force relations of single experiments. Then, we find most stiffening exponents in a range between 0.5 and 2, but also detect outliers below this range and close to 4, Fig. 3F.

For a better visibility and comparability of the strain stiffening of the different Ndc80 variants, we summarize the stiffness measurements in Fig. 3G by binning the time-traced stiffnesses of all experiments in bins of $1\,\mathrm{pN}$ width and averaging force and stiffness in each of these bins. We find that all variant Ndc80 complexes exhibit similar strain stiffening. Both truncating the tail or modifying the CH domain slightly decrease the stiffness compared to the wild type, especially for small forces. This indicates that in all four Ndc80 variants, the remaining intact common parts play a central role in strain stiffening. Differences between variants are due to changes in the Ndc80–MT bond and will be addressed in the Discussion section.

Measured stiffness is independent of MT state

When a MT is rescued after the stall, as in the experiment depicted in Fig. 3C, the time-traced stiffness follows the same stiffness–force relation in the shrinking and growing states before and after rescue, respectively. The same observation can be made in experiments with several consecutive rescues and catastrophes. This indicates that the stiffness is independent of the MT state, i.e., on whether the Ndc80 complexes are attached to a shrinking, stalled, or growing MT. To address this question systematically, we identify the phases of shrinking, stalled and growing MTs in the single experiments, and bin the stiffnesses analogously to Fig. 3G but separately for each of the three MT states. The results in Fig. 3H do not show a significant dependence on the MT state for any of the four Ndc80 variants. The independence of Ndc80-MT linker stiffness from MT state indicates that PFs either do not contribute to the total stiffness (because $c_{\mathrm{PF}} \gg c_{\mathrm{tot}}$), or that, if they do contribute, their mechanical properties do not depend on whether the MT is growing or shrinking. The stiffness contributions of PFs are investigated below in more detail.

PLL-PEG is too stiff to contribute to the measured stiffnesses

In the following sections, we attempt to explain the observed strain stiffening by modeling the elastic elements between the bead and the MT that add up to the stiffness $\tilde{c}(F)$ as shown in Fig. 2B and Eq. 2. We start with the PLL-PEG linkage to the bead, whose contribution to the measured stiffnesses should be clarified in addition to those from the Ndc80 complex or the PF. PLL-PEG consists of a poly-L-lysine (PLL) backbone and polyethylene glycol (PEG) side chains. While the PLL backbone is adsorbed on the glass bead in the experiment, the flexible PEG chains can bind the Ndc80 oligomers.

From force–extension curves measured in AFM experiments (34), stiffness of PLL adsorbed on a flat Nb_2O_5 surface can be estimated as $\sim 100\,\mathrm{pN\,nm^{-1}}$ which is three orders of magnitude above the stiffnesses observed in our experiments. Oesterhelt *et al.* (32) successfully described the elasticity of single PEG polymers by means of an extended FJC model with a bond length that follows from a two-level system. Applying this model to the PEG-2000 with $N_{\mathrm{S}} = 45$ segments used in our experiments, we obtain a force-free stiffness of $1.38\,\mathrm{pN\,nm^{-1}}$, that increases under tension as shown in the Supporting Material.

We conclude that both the PLL backbone and the PEG chains are too stiff to make a significant contribution to the observed strain stiffening and can be omitted in the following analysis ($c_{\mathrm{PEG}}(F) \gg \tilde{c}(F)$ in Eq. 2.

Stiffening is a direct consequence of the Ndc80 structure

Next, we consider the Ndc80 complex modeled as a FJC with two flexibly connected stiff arms (see Fig. 2C), resulting in a stiffness $c_{\mathrm{Ndc}}(F)$ as given by Eq. 8. We have to take into account that there might be n Ndc80 complexes attached in parallel. For this situation, we assume that each Ndc80 complex has the same elongation so that the force F is shared equally by the attached complexes and the total stiffness is given by $n\,c_{\mathrm{Ndc}}(F/n)$ (see Eq. 3). In Fig. 4A, we compare the total stiffness of n

parallel Ndc80 complexes to the measured stiffnesses of Ndc80^{wt}. For any n, the model results are about a factor 2-4 larger than the measured values. Moreover, the two-segment Ndc80 model results in a strain stiffening exponent $m = 2$ in Eq. 9, which is larger than the measured values $m \approx 1$ in Fig. 3E. We conclude that the stiffness of the Ndc80 complex alone can explain strain stiffening but is not sufficient to explain the measured stiffnesses quantitatively.

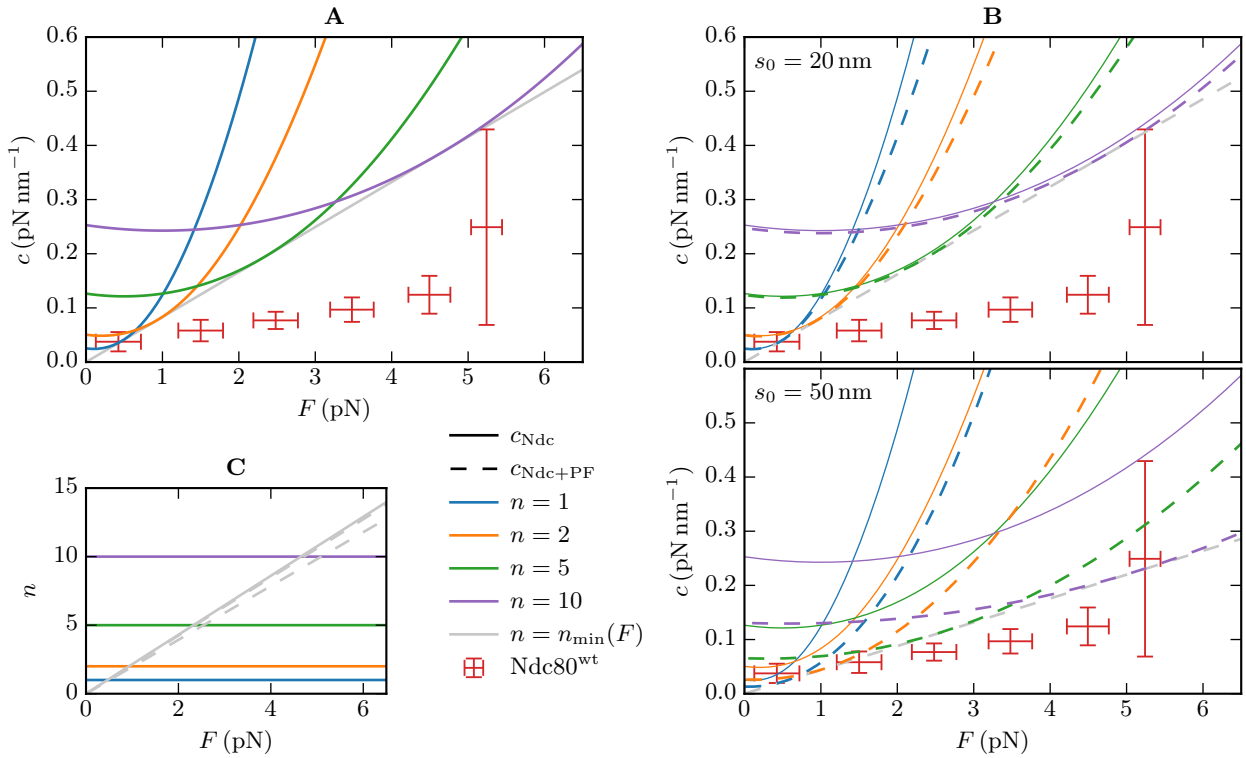

Figure 4: (A) The stiffness of n parallel Ndc80 complexes $n\,c_{\mathrm{Ndc}}(F/n)$ according to Eq. 7 (colored lines) is by a factor of 2-4 larger than the measurements with wild type Ndc80. The theoretical stiffness is minimized when the number of attached Ndc80 complexes increases linearly with the force ($n_{\min}(F)$, gray line). (B) Stiffness of n parallel Ndc80 complexes each in series with a PF (dashed lines). Top: When the attachment on the curved PF has a distance of $s_0 = 20\,\mathrm{nm}$ from the straight MT lattice, the stiffness only differs slightly from the bare Ndc80 stiffness (solid lines). Bottom: For $s_0 = 20\,\mathrm{nm}$ the PF does have a significant contribution to the total stiffness. However, the combined stiffnesses of Ndc80 complexes and PFs are still larger than the experimental outcomes for wild type Ndc80. (C) Force-dependent number of attached Ndc80 complexes that minimizes the theoretical stiffness ($n_{\min}(F)$, gray).

The fact that the Ndc80 model gives larger stiffnesses than measured motivates the consideration of the additional elastic elements from the Ndc80–MT bond and the PFs in the total stiffness in Eq. 2. These elements are in series to the Ndc80 complex and potentially reduce the total stiffness of the entire Ndc80–MT link.

Only long protofilaments are flexible enough to reduce the total stiffness

We assume that forces recorded in our experiments are produced by tubulin protofilaments bending outwards from the MT lattice when a MT shortens. We always record stall events after a force has been developed, i.e. we do not observe bead-bound Ndc80 preventing MT shortening without force development. Therefore, we hypothesize that bead-bound Ndc80 interacts with bent protofilaments during stall. We also assume that during stall, the MT-generated force is equalized by the returning force of the optical trap directed along the MT axis in the opposite direction.

Since the PFs are bent out of their preferred curvature, a restoring force on the Ndc80 complexes builds up, governed by an effective stiffness c_{PF} for strains in the axial direction. In the Materials and Methods section, we quantified this stiffness with a simple beam model (see Fig. 2D) in Eq. 11. This model depends on three parameters: the preferred curvature ϕ of the PF, its persistence length L_{p} that defines the bending stiffness $\alpha = k_{\mathrm{B}}TL_{\mathrm{p}}$, and the position s_0 along the free part of the PF where the Ndc80 complex attaches, i.e., where the force is applied. While the first two parameters as well as the length of the free curved parts of the PF are well described for MTs in vitro (31), a fixed attachment position s_0 of Ndc80 complex to the PF is

not known, and we use typical values $s_0 = 20\,\mathrm{nm}$ and $s_0 = 50\,\mathrm{nm}$.

In Fig. 4B, we plotted the stiffnesses of n parallel Ndc80 complexes with c_{Ndc} that are each in series with a PF c_{PF}. We see that the influence of PF bending is negligible for $s_0 = 20\,\mathrm{nm}$, whereas for $s_0 = 50\,\mathrm{nm}$ the PF significantly reduces the total stiffness. We conclude that the PF stiffness is only relevant, when the Nd80 complex is attached near the end of a sufficiently long PF. An upper bound for s_0 is given by the total length of the curved part of the PF for which values of $L = 10\text{-}80\,\mathrm{nm}$ have been measured in vitro (31).

However, even when long PFs are considered, the additional PF elasticity does not lower the calculated stiffness sufficiently to accurately describe the experimental outcomes. This motivates the last step of our analysis.

Catch bond behavior lowers the stiffness of parallel Ndc80 complexes

So far, we have assumed a *fixed* number n of parallel Ndc80 complexes over the whole range of applied forces. We now analyze how our model behaves when the number n of attached Ndc80 complexes depends on the applied force, $n = n(F)$. In principle, both a catch bond and a slip bond mechanism are conceivable for the Ndc80–MT bond. A catch (slip) bond is characterized by a binding affinity that increases (decreases) under tension (35). In our model, a catch (slip) bond implies a monotonically increasing (decreasing) force-dependent number of attached Ndc80 complexes $n(F)$.

We find that a force-dependent $n(F)$ can lower the effective total stiffness of the entire Ndc80–MT link. The minimal cooperative stiffness that can be realized is the envelope of the stiffness–force relations $c_n(F)$ for different n in Fig. 4AB. The envelope of the $c_n(F)$ relations is obtained by a force-dependent number $n_{\min}(F)$ of attached Ndc80 complexes that minimizes the stiffness $c_n(F)$ for each F. The resulting $n_{\min}(F)$ is shown in Fig. 4C and increases linearly in the examined force range, which also implies a catch bond behavior. For long PFs ($s_0 = 50\,\mathrm{nm}$), the envelope stiffness $c_{n_{\min}}(F)$ has actually the correct order of magnitude as compared to the experimental data shown in Fig. 4B. The number $n_{\min}(F)$ also remains below $n = 15$ in the examined force range, which is in agreement with estimates for the number of Ndc80 complexes in the proximity of the MT given the expected Ndc80 density on the bead (5, 7).

Apart from the absolute stiffness values, a model should reproduce the observed roughly linear strain stiffening behavior with the exponent m around unity (see Fig. 3E). The relation $n(F)$ can change the strain stiffening exponents which are $m = 2$ for the Ndc80 stiffness (Eq. 9) and $m = 2.5$ for the PF (Eq. 12). From Eq. 3, one can see that a linearly increasing $n(F)$ actually implies a linear stiffening as observed in our experiments since $F/n(F) = \mathrm{const}$ and, therefore, $\tilde{c}_n(F) = n(F)\tilde{c}(\mathrm{const}) \propto n(F)$.

For a slip bond, on the other hand, where $\partial_F n(F) < 0$ and $n(F) \to 0$ for large forces by definition, the argument in Eq. 3, $F/n(F)$, increases rapidly. As a consequence, we can approximate c_{Ndc} and c_{PF} with the power laws from Eqs. 9 and 12, respectively, so that

$$c_n(F) \sim n(F)\left(\frac{F}{n(F)}\right)^m = \frac{F^m}{(n(F))^{m-1}} > \mathcal{O}(F^m), \tag{14}$$

We conclude that any kind of slip bond will increase the stiffening exponent for large forces. Stiffening exponents below the values $m = 2$ for Ndc80 stiffness or $m = 2.5$ for PF stiffness, as obtained in the experiments, are indicative of a catch bond mechanism. For the time traces from single experiments in Fig. 3F, 79 % of the stiffening exponents lie below 2.

DISCUSSION

The novel analysis of time traces of bead positions in optical trapping experiments allows us to time-trace the stiffness during single experiments and go beyond an analysis limited to the MT stall state (7). This enabled us to increase the available number of stiffness measurements by 1 to 2 orders of magnitude and study strain stiffening of wild type Ndc80 in more detail. It also enabled us to study strain stiffening of Ndc80 variants with a truncated tail or with a mutated CH domain, both of which typically detach before the MT has been stalled, and to explore strain stiffening selectively in the shrinking, stalled and growing state of MTs.

We found that all mutant Ndc80 complexes exhibit strain stiffening hinting at a central role of the Ndc80–Nuf2 coiled coil, rather than the MT binding sites in the CH-domain and the N-terminal tail. The measured stiffnesses of the entire Ndc80–MT link are lower than theoretical predictions from our Ndc80 model. Therefore, additional elastic elements in the Ndc80–MT link or a force-dependent number of attached Ndc80 complexes should be relevant. We could exclude the PLL-PEG connection between Ndc80 complexes and the bead, which is too stiff to contribute. Effects from protofilament flexibility and an increasing number of attached Ndc80 complexes under force (catch bond) are necessary for the model to conform to experimentally measured stiffnesses. Moreover, stiffness differences between variants allow us to draw some conclusions on the Ndc80–MT bond.

Effects from protofilaments

Time-tracing of the stiffness allowed us to study strain stiffening selectively in the shrinking, stalled and growing state of MTs. We found no significant stiffness differences between MT states (see Figs. 3C and H) leading to the conclusion that the stiffness of the bent PFs is either too large to contribute significantly to the total stiffness or that it does not depend on the MT's polymerization state.

Our PF model showed that the PF contribution to the overall stiffness depends strongly on the length of the PFs and the position along the PF where the Ndc80 complex is attached. An attachment point s_0 close to the straight part of the PF ($s_0 \leq 20\,\mathrm{nm}$) predicts a negligible contribution of the PF. Indeed, single Ndc80 complexes are only able to bind to straight but not to curved PFs (6). However, our stiffness measures derive from experiments where Ndc80 multimers were used that were able to tip-track—in contrast to the single Ndc80 complexes in Ref. (6)—and that could be bound to more curved segments of the MT end.

Attachment of Ndc80 to long flaring PFs with attachment lengths around $s_0 = 50\,\mathrm{nm}$ are predicted to reduce the stiffness of the Ndc80–MT link to values close to the measured stiffnesses (Fig. 4B). This favors the second possible explanation, namely that PFs contribute to the total stiffness but have identical elastic properties during MT shrinkage, stall and growth. This is also in agreement with the recent observation that the curvature of PFs is the same during polymerization and depolymerization (31).

Ndc80 has not been observed to interact with bent tubulin (6, 36). Therefore, the interaction that we propose between the Ndc80 and the bent protofilaments at the shortening MT end should be transient and only happening during stalled depolymerization. Alternatively, the stiffening of the Ndc80–MT connection might arise from force-dependent changes of thermal diffusion of Ndc80 along the cylindrical part of the MT near the protofilament flare, without a direct interaction with bent protofilaments (37). We did not explore this possibility in the model because parameters of Ndc80 diffusion as a function of force are not available from published experimental data.

Number of attached Ndc80 complexes and potential catch bond mechanism

The number n of simultaneously attached Ndc80 complexes could not be directly inferred from the experiments in Refs. (7, 10). From the known Ndc80 densities on the bead we can estimate that 1 to 4 Ndc80 trimers, i.e., 3 to 12 Ndc80 complexes are in the vicinity of the MT end and can potentially bind (7).

From the equal stiffness–force relations before and after a rescue, we conclude that also the number of attached Ndc80 complexes is the same during polymerization and depolymerization. Dynamically, it is possible that the number of attached Ndc80 complexes changes in a force-dependent manner between MT catastrophes and rescues. For force-free detachment and attachment of a single $\mathrm{Ndc80^{wt}}$ complex, time scales of $\tau_{\mathrm{off}} = 1.6\,\mathrm{s}$ and $\tau_{\mathrm{on}} = 0.4\,\mathrm{s}$, respectively, have been found (7). With a phosphorylated tail, τ_{off} is supposed to be smaller (12). Since the durations of MT depolymerization vary in a wide range from less than $1\,\mathrm{s}$ up to $\sim 100\,\mathrm{s}$, both a constant and a dynamic number of attached complexes are possible.

Our modeling results showed that the absolute stiffness values as well as the roughly linear strain stiffening relation (see Fig. 3E) are best reproduced by a force-dependent number $n(F)$, which increases linearly with force (see Fig. 4B) implying a catch bond mechanism. Among the stiffening exponents for the time traces from single experiments in Fig. 3F, 79 % of the strain stiffening exponents lie below 2, which is indicative of a catch bond like behavior.

Assuming that Ndc80 forms a catch bond to the MT, the question arises how this mechanism could work. The whole kinetochore, consisting of several additional proteins, has been proposed to act like a catch bond (38). It is widely assumed that the Aurora B kinase, which was not present in our experiments, is important in the kinetochore's catch bond mechanism (39–41). Kinetochores purified from S. cerevisiae, however, were shown to build catch bonds with MTs in vitro even without Aurora B activity (42). Importantly, the catch-bond behavior of the purified yeast kinetochores was abolished when Dam1 or Stu2 were absent, even in presence of Ndc80 (42, 43). There is evidence that Ndc80 stretching correlates with MT binding as the Ndc80 complex may exist in an auto-inhibited bent conformation with reduced MT binding capacity (44) and that the Ndc80 complex bends ("jackknifes") upon detachment (45). This suggests that the binding affinity for MTs increases when the Ndc80 complex is stretched, which would further imply that Ndc80 has an intrinsic catch-bond-like mechanism. To what extent this effect is relevant for our experiments is unclear, as according to our FJC model the Ndc80 complex is already stretched by small forces. For instance, at $F = 1\,\mathrm{pN}$ we find a mean angle of $(44 \pm 23)^\circ$ between the arms $\vec{a}$ and $\vec{b}$ (where the angle is 0° for a maximally stretched Ndc80 complex). Speculating on other possible catch bond mechanisms, it is conceivable that by stretching the unstructured tail additional binding sites become available which are concealed in the entangled tail at low forces. Force-enhanced adhesion by unfolding is a common catch bond mechanism (46); examples are the von Willebrand factor (47, 48) and α-catenin bonding to F-actin (49) in the cytoskeleton. In conclusion, an intrinsic catch bond mechanism of Ndc80 complexes is compatible with current knowledge and worth considering as one of the ingredients that define the characteristics of Ndc80 strain stiffening. Such a mechanism could also contribute to the catch bond behavior of the entire kinetochore.

Structure of Ndc80–MT bond and role of the N-terminal tail in MT binding

Stiffness differences between the wild type Ndc80^{wt} and mutants $\text{Ndc80}^{\Delta 80}$ and $\text{Ndc80}^{\text{CHmut}}$ reflect roles in MT binding of the the N-terminal tail and the CH domain, respectively. These differences will allow us to draw some conclusions on the Ndc80–MT bond, whose exact mechanism is still unknown. The CH domain binds between two tubulin monomers via a structural element named the "toe"(27). The N-terminal tail also supports MT binding, but its exact role is still under debate. Three models are currently discussed (23, 50): direct binding to the MT lattice, cooperativity and clustering by interactions with neighboring Ndc80 complexes, and co-factor recruitment. Since no co-factors were present in our experiments, we will concentrate on the former two models.

Our comparative study of Ndc80^{wt}, $\text{Ndc80}^{\Delta 80}$ and $\text{Ndc80}^{\text{CHmut}}$ allows us to dissect the role of the tail and the CH domain on Ndc80–MT binding. Both Ndc80 mutants displayed decreased stiffnesses compared to the wild type (Fig. 3G), an effect we ascribed either to a softened Ndc80–MT bond or to a reduced number of attached Ndc80 complexes. In the elastic toy model in Fig. 5A, both the CH domain and the tail of Ndc80^{wt} bind to the PF, so that they can be represented by two parallel springs that add up to the total bond stiffness c_{bond}. Due to the parallel arrangement, lack of either of the two springs in $\text{Ndc80}^{\Delta 80}$ or $\text{Ndc80}^{\text{CHmut}}$ reduces the bond stiffness, predicting overall stiffnesses as depicted in Fig. 3G. If both the CH domain and the N-terminal tail bind directly to the MT lattice, the two Ndc80 mutants probably have a reduced MT binding affinity. Therefore, in the direct binding model, the reduction of the overall stiffness could be a consequence of a reduced number of attached Ndc80 complexes as well as of a reduction of the individual bond stiffnesses.

When the N-terminal tail interacts with neighboring Ndc80 complexes instead of the tubulin, the induced cooperativity supports parallel attachments of multiple Ndc80^{wt} complexes, see Fig. 5B. Deletion of the tail or mutation of the CH domain may impair the cooperative behavior, with the result that fewer linkers connect the bead (or the kinetochore) with the MT and the overall stiffness decreases. While there is evidence supporting a contribution of the tail to cooperative MT binding, there is at present no clear evidence indicating that the Ndc80 CH domain contributes to binding cooperativity.

Tail phosphorylation was shown to reduce the MT binding affinity of the Ndc80 complex (2, 11–14). Moreover, the durations of the MT stalls are shorter when the Ndc80 tails are phosphorylated (10). This suggests that phosphorylation impedes the function of the tail similarly as if the tail is truncated. However, in contrast to $\text{Ndc80}^{\Delta 80}$, the stiffness of Ndc80^{P} is not significantly reduced compared to Ndc80^{wt}, see Fig. 3G. It remains an open question how these observations are compatible with the binding models depicted in Fig. 5.

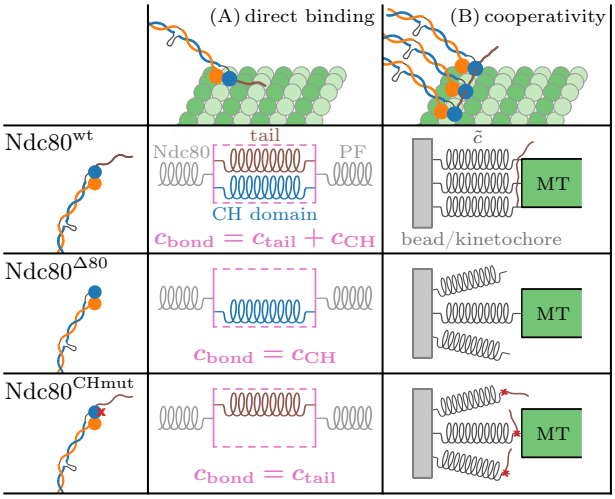

Figure 5: Models of the Ndc80–MT bond for potential roles of the N-terminal tail. (A) When the tail binds directly to the PF, an elastic model of the Ndc80–MT bond comprises the tail and the CH domain as two parallel springs. If the tail is deleted ($\text{Ndc80}^{\Delta 80}$) or the CH binding domain is blocked ($\text{Ndc80}^{\text{CHmut}}$), either of those springs is missing which lowers the bond stiffness c_{bond} and thereby the total stiffness $\tilde{c}$. (B) In the case of an interaction of the tail with CH domains of neighboring Ndc80 complexes, the number of parallelly attached linkers is reduced for the two mutants $\text{Ndc80}^{\Delta 80}$ and $\text{Ndc80}^{\text{CHmut}}$.

Comparison of model and experiment

Our model can explain the strain stiffening from the structure of the Ndc80 complex and the bending elasticity of long flaring PFs. If we allow for a force-dependent number of bound Ndc80 complexes, a linearly increasing number of bound complexes (requiring a catch bond mechanism) also reproduces the observed roughly linear strain stiffening relation. Ndc80, by itself or in series with PFs, gives absolute stiffness values that are still above the measured stiffnesses. Including a force-dependent number of bound Ndc80 complexes gives values which are close but still slightly higher than measured. As already mentioned, the missing part might be the Ndc80–MT bond, which is additionally in series with the Ndc80 complex and the PF as illustrated in Fig. 2. However, since the stiffness of the bond is hard to quantify due to the little knowledge of the exact binding mechanism, we did not go beyond the qualitative discussion in the previous section.

Regarding the Ndc80, we have also investigated possible effects from finite flexibility of the two Ndc80 arms by modeling both arms as semiflexible worm-like chains. We performed Monte Carlo simulations, in which each Ndc80 arm had the same persistence length L_p. Using persistence lengths in a realistic range of $L_\mathrm{p} \gtrsim 100\,\mathrm{nm}$ as they have been determined for other coiled coil proteins such as tropomyosin (51), our simulations lead to the conclusion that semiflexibility has only a minor effect on total stiffness (see Supporting Material).

Finally, we need to discuss the accuracy of our experimental method. While the trap stiffness was calibrated by fitting the power spectrum based on Brownian motion in a harmonic potential (52–54), this well-established method can not be applied for measurements of the anharmonic Ndc80 stiffness. Therefore, we had to determine the Ndc80 stiffness from the variance of bead position, which is a simpler and universal but less accurate approach. In particular, the measured overall variance contains a systematic noise that is added to the actual variance of bead position, which is why the stiffness tends to be underestimated by $k_\mathrm{B}T/\mathrm{Var}(x)$ (55–57). This systematic underestimation, which we can not quantify, might explain why our model tends to predict higher stiffnesses than experimentally measured.

CONCLUSION

In conclusion, we accumulated extensive stiffness data of the Ndc80–MT link by optical trapping methods in combination with a novel time-tracing analysis. We were able to study Ndc80 complexes and three variants. Our theoretical model for the Ndc80–MT link consisting of a mechanical model of the Ndc80 complex and flaring PFs at the MT tip is able to explain the strain stiffening and reproduces the correct order of magnitude of the stiffness. The theoretical model is based on the known structural features of the Ndc80 complex and of the PFs at the MT tip. Thus, our results on the elastic properties further support these structural models from the mechanical point of view. Our model also reproduces the roughly linear strain stiffening behavior when taking a force-dependent binding affinity into account.

AUTHOR CONTRIBUTIONS

A.M., M.D., V.A.V. and P.J.H. conceived and designed the experiments. P.J.H. contributed reagents. V.A.V. performed and analyzed the experiments. J.K. and F.S. developed the theoretical model. F.S. analyzed the data and performed calculations. F.S. and J.K. wrote the original draft. A.M., V.A.V. and P.J.H. reviewed and edited the manuscript.

ACKNOWLEDGMENTS

V.A.V. and M.D. acknowledge support from European Research Council Synergy Grant MODELCELL (proposal 609822). A.M. acknowledges funding by European Research Council (ERC) through Synergy Grant 951439 (BIOMECANET).

SUPPORTING MATERIAL

Supporting Material can be found online at http://www.biophysj.org.

SUPPORTING CITATIONS

References (58–60) appear in the Supporting material.

REFERENCES

1. Musacchio, A., and A. Desai, 2017. A Molecular View of Kinetochore Assembly and Function. *Biology* 6:5. http://www.mdpi.com/2079-7737/6/1/5.

2. DeLuca, J. G., W. E. Gall, C. Ciferri, D. Cimini, A. Musacchio, and E. D. Salmon, 2006. Kinetochore Microtubule

Dynamics and Attachment Stability Are Regulated by Hec1. *Cell* 127:969–982. https://linkinghub.elsevier.com/retrieve/pii/S0092867406014085.

3. Wei, R. R., P. K. Sorger, and S. C. Harrison, 2005. Molecular organization of the Ndc80 complex, an essential kinetochore component. *Proceedings of the National Academy of Sciences of the United States of America* 102:5363–5367. http://www.pnas.org/cgi/doi/10.1073/pnas.0501168102.

4. Wang, H.-W., S. Long, C. Ciferri, S. Westermann, D. Drubin, G. Barnes, and E. Nogales, 2008. Architecture and Flexibility of the Yeast Ndc80 Kinetochore Complex. *Journal of Molecular Biology* 383:894–903. https://linkinghub.elsevier.com/retrieve/pii/S0022283608011017.

5. Powers, A. F., A. D. Franck, D. R. Gestaut, J. Cooper, B. Gracyzk, R. R. Wei, L. Wordeman, T. N. Davis, and C. L. Asbury, 2009. The Ndc80 Kinetochore Complex Forms Load-Bearing Attachments to Dynamic Microtubule Tips via Biased Diffusion. *Cell* 136:865–875. https://linkinghub.elsevier.com/retrieve/pii/S0092867409000233.

6. Schmidt, J. C., H. Arthanari, A. Boeszoermenyi, N. M. Dashkevich, E. M. Wilson-Kubalek, N. Monnier, M. Markus, M. Oberer, R. A. Milligan, M. Bathe, G. Wagner, E. L. Grishchuk, and I. M. Cheeseman, 2012. The Kinetochore-Bound Ska1 Complex Tracks Depolymerizing Microtubules and Binds to Curved Protofilaments. *Developmental Cell* 23:968–980. https://linkinghub.elsevier.com/retrieve/pii/S1534580712004236.

7. Volkov, V. A., P. J. Huis in 't Veld, M. Dogterom, and A. Musacchio, 2018. Multivalency of NDC80 in the outer kinetochore is essential to track shortening microtubules and generate forces. *eLife* 7:e36764. https://elifesciences.org/articles/36764.

8. Tien, J. F., N. T. Umbreit, D. R. Gestaut, A. D. Franck, J. Cooper, L. Wordeman, T. Gonen, C. L. Asbury, and T. N. Davis, 2010. Cooperation of the Dam1 and Ndc80 kinetochore complexes enhances microtubule coupling and is regulated by aurora B. *Journal of Cell Biology* 189:713–723. https://rupress.org/jcb/article/189/4/713/35839/Cooperation-of-the-Dam1-and-Ndc80-kinetochore.

9. Lampert, F., P. Hornung, and S. Westermann, 2010. The Dam1 complex confers microtubule plus end–tracking activity to the Ndc80 kinetochore complex. *Journal of Cell Biology* 189:641–649. https://rupress.org/jcb/article/189/4/641/35836/The-Dam1-complex-confers-microtubule-plus.

10. Huis in 't Veld, P. J., V. A. Volkov, I. D. Stender, A. Musacchio, and M. Dogterom, 2019. Molecular determinants of the Ska-Ndc80 interaction and their influence on microtubule tracking and force-coupling. *eLife* 8:e49539. https://elifesciences.org/articles/49539.

11. DeLuca, K. F., S. M. A. Lens, and J. G. DeLuca, 2011. Temporal changes in Hec1 phosphorylation control kinetochore-microtubule attachment stability during mitosis. *Journal of Cell Science* 124:622–634. http://jcs.biologists.org/cgi/doi/10.1242/jcs.072629.

12. Umbreit, N. T., D. R. Gestaut, J. F. Tien, B. S. Vollmar, T. Gonen, C. L. Asbury, and T. N. Davis, 2012. The Ndc80 kinetochore complex directly modulates microtubule dynamics. *Proceedings of the National Academy of Sciences* 109:16113–16118. http://www.pnas.org/cgi/doi/10.1073/pnas.1209615109.

13. Zaytsev, A. V., L. J. Sundin, K. F. DeLuca, E. L. Grishchuk, and J. G. DeLuca, 2014. Accurate phosphoregulation of kinetochore–microtubule affinity requires unconstrained molecular interactions. *Journal of Cell Biology* 206:45–59. https://rupress.org/jcb/article/206/1/45/37588/Accurate-phosphoregulation-of.

14. DeLuca, K. F., A. Meppelink, A. J. Broad, J. E. Mick, O. B. Peersen, S. Pektas, S. M. Lens, and J. G. DeLuca, 2018. Aurora A kinase phosphorylates Hec1 to regulate metaphase kinetochore–microtubule dynamics. *Journal of Cell Biology* 217:163–177. https://rupress.org/jcb/article/217/1/163/39165/Aurora-A-kinase-phosphorylates-Hec1-to-regulate.

15. Hill, T. L., 1985. Theoretical problems related to the attachment of microtubules to kinetochores. *Proceedings of the National Academy of Sciences of the United States of America* 82:4404–4408. http://www.pnas.org/cgi/doi/10.1073/pnas.82.13.4404.

16. Joglekar, A. P., and A. J. Hunt, 2002. A Simple, Mechanistic Model for Directional Instability during Mitotic Chromosome Movements. *Biophysical Journal* 83:42–58. https://linkinghub.elsevier.com/retrieve/pii/S0006349502751485.

17. Civelekoglu-Scholey, G., D. J. Sharp, A. Mogilner, and J. M. Scholey, 2006. Model of Chromosome Motility in Drosophila Embryos: Adaptation of a General Mechanism for Rapid Mitosis. *Biophysical Journal* 90:3966–3982. https://linkinghub.elsevier.com/retrieve/pii/S0006349506725796.

18. Gay, G., T. Courtheoux, C. Reyes, S. Tournier, and Y. Gachet, 2012. A stochastic model of kinetochore–microtubule attachment accurately describes fission yeast chromosome segregation. *Journal of Cell Biology* 196:757–774. https://rupress.org/jcb/article/196/6/757/36929/A-stochastic-model-of-kinetochoremicrotubule.

19. Civelekoglu-Scholey, G., B. He, M. Shen, X. Wan, E. Roscioli, B. Bowden, and D. Cimini, 2013. Dynamic bonds and polar ejection force distribution explain kinetochore oscillations in PtK1 cells. *Journal of Cell Biology* 201:577–593.

20. Keener, J. P., and B. Shtylla, 2014. A Mathematical Model of Force Generation by Flexible Kinetochore-Microtubule Attachments. *Biophysical Journal* 106:998–1007. https://linkinghub.elsevier.com/retrieve/pii/S0006349514000812.

21. Banigan, E. J., K. K. Chiou, E. R. Ballister, A. M. Mayo, M. A. Lampson, and A. J. Liu, 2015. Minimal model for collective kinetochore–microtubule dynamics. *Proceedings of the National Academy of Sciences* 112:12699–12704. http://www.pnas.org/lookup/doi/10.1073/pnas.1513512112.

22. Schwietert, F., and J. Kierfeld, 2020. Bistability and oscillations in cooperative microtubule and kinetochore dynamics in the mitotic spindle. *New Journal of Physics* 22:053008. https://iopscience.iop.org/article/10.1088/1367-2630/ab7ede.

23. Ciferri, C., S. Pasqualato, E. Screpanti, G. Varetti, S. Santaguida, G. Dos Reis, A. Maiolica, J. Polka, J. G. De Luca, P. De Wulf, M. Salek, J. Rappsilber, C. A. Moores, E. D. Salmon, and A. Musacchio, 2008. Implications for Kinetochore-Microtubule Attachment from the Structure of an Engineered Ndc80 Complex. *Cell* 133:427–439. https://linkinghub.elsevier.com/retrieve/pii/S0092867408004017.

24. Weissmann, F., G. Petzold, R. VanderLinden, P. J. Huis in 't Veld, N. G. Brown, F. Lampert, S. Westermann, H. Stark, B. A. Schulman, and J.-M. Peters, 2016. biGBac enables rapid gene assembly for the expression of large multisubunit protein complexes. *Proceedings of the National Academy of Sciences* 113:E2564–E2569. http://www.pnas.org/lookup/doi/10.1073/pnas.1604935113.

25. Fairhead, M., G. Veggiani, M. Lever, J. Yan, D. Mesner, C. V. Robinson, O. Dushek, P. A. van der Merwe, and M. Howarth, 2014. SpyAvidin Hubs Enable Precise and Ultrastable Orthogonal Nanoassembly. *Journal of the American Chemical Society* 136:12355–12363. https://pubs.acs.org/doi/10.1021/ja505584f.

26. Wei, R. R., J. Al-Bassam, and S. C. Harrison, 2007. The Ndc80/HEC1 complex is a contact point for kinetochore-microtubule attachment. *Nat. Struct. Mol. Biol.* 14:54–59.

27. Alushin, G. M., V. H. Ramey, S. Pasqualato, D. A. Ball, N. Grigorieff, A. Musacchio, and E. Nogales, 2010. The Ndc80 kinetochore complex forms oligomeric arrays along microtubules. *Nature* 467:805–810. http://www.nature.com/articles/nature09423.

28. DeLuca, J. G., and A. Musacchio, 2012. Structural organization of the kinetochore–microtubule interface. *Curr. Opin. Cell Biol.* 24:48–56. http://dx.doi.org/10.1016/j.ceb.2011.11.003https://linkinghub.elsevier.com/retrieve/pii/S0955067411001499.

29. Flory, P. J., 1969. Statistical mechanics of chain molecules. Interscience Publishers, New York.

30. Kierfeld, J., O. Niamploy, V. Sa-yakanit, and R. Lipowsky, 2004. Stretching of semiflexible polymers with elastic bonds. *The European Physical Journal E* 14:17–34. http://link.springer.com/10.1140/epje/i2003-10089-3.

31. McIntosh, J. R., E. O'Toole, G. Morgan, J. Austin, E. Ulyanov, F. Ataullakhanov, and N. Gudimchuk, 2018. Microtubules grow by the addition of bent guanosine triphosphate tubulin to the tips of curved protofilaments. *Journal of Cell Biology* 217:2691–2708. https://rupress.org/jcb/article/217/8/2691/39547/Microtubules-grow-by-the-addition-of-bent.

32. Oesterhelt, F., M. Rief, and H. E. Gaub, 1999. Single molecule force spectroscopy by AFM indicates helical structure of poly(ethylene-glycol) in water. *New Journal of Physics* 1:6.1–6.11. https://iopscience.iop.org/article/10.1088/1367-2630/1/1/006.

33. Huber, P. J., 1964. Robust Estimation of a Location Parameter. *The Annals of Mathematical Statistics* 35:73–101. http://projecteuclid.org/euclid.aoms/1177703732.

34. Pasche, S., M. Textor, L. Meagher, N. D. Spencer, and H. J. Griesser, 2005. Relationship between Interfacial Forces Measured by Colloid-Probe Atomic Force Microscopy and Protein Resistance of Poly(ethylene glycol)-Grafted Poly(L-lysine) Adlayers on Niobia Surfaces. *Langmuir* 21:6508–6520. https://pubs.acs.org/doi/10.1021/la050386x.

35. Thomas, W. E., V. Vogel, and E. Sokurenko, 2008. Biophysics of Catch Bonds. *Annu. Rev. Biophys.* 37:399–416. http://www.annualreviews.org/doi/10.1146/annurev.biophys.37.032807.125804.

36. Volkov, V. A., P. M. Grissom, V. K. Arzhanik, A. V. Zaytsev, K. Renganathan, T. McClure-Begley, W. M. Old, N. Ahn, and J. R. McIntosh, 2015. Centromere protein F includes two sites that couple efficiently to depolymerizing microtubules. *Journal of Cell Biology* 209:813–828. https://rupress.org/jcb/article/209/6/813/38153/Centromere-protein-F-includes-two-sites-that.

37. Grishchuk, E. L., 2017. Biophysics of Microtubule End Coupling at the Kinetochore. *In* Progress in Molecular and Subcellular Biology, NLM (Medline), volume 56, 397–428. http://link.springer.com/10.1007/978-3-319-58592-5{_}17.

38. Sarangapani, K. K., and C. L. Asbury, 2014. Catch and release: how do kinetochores hook the right microtubules during mitosis? *Trends in Genetics* 30:150–159. https://linkinghub.elsevier.com/retrieve/pii/S0168952514000274.

39. Liu, D., G. Vader, M. J. M. Vromans, M. A. Lampson, and S. M. A. Lens, 2009. Sensing Chromosome Bi-Orientation by Spatial Separation of Aurora B Kinase from Kinetochore Substrates. *Science* 323:1350–1353. https://www.sciencemag.org/lookup/doi/10.1126/science.1167000.

40. Caldas, G. V., K. F. DeLuca, and J. G. DeLuca, 2013. KNL1 facilitates phosphorylation of outer kinetochore proteins by promoting Aurora B kinase activity. *Journal of Cell Biology* 203:957–969. https://rupress.org/jcb/article/203/6/957/37698/KNL1-facilitates-phosphorylation-of-outer.

41. Yoo, T. Y., J.-M. Choi, W. Conway, C.-H. Yu, R. V. Pappu, and D. J. Needleman, 2018. Measuring NDC80 binding reveals the molecular basis of tension-dependent kinetochore-microtubule attachments. *eLife* 7:1–34. https://elifesciences.org/articles/36392.

42. Akiyoshi, B., K. K. Sarangapani, A. F. Powers, C. R. Nelson, S. L. Reichow, H. Arellano-Santoyo, T. Gonen, J. A. Ranish, C. L. Asbury, and S. Biggins, 2010. Tension directly stabilizes reconstituted kinetochore-microtubule attachments. *Nature* 468:576–579. http://www.nature.com/articles/nature09594.

43. Miller, M. P., C. L. Asbury, and S. Biggins, 2016. A TOG Protein Confers Tension Sensitivity to Kinetochore-Microtubule Attachments. *Cell* 165:1428–1439. http://dx.doi.org/10.1016/j.cell.2016.04.030https://linkinghub.elsevier.com/retrieve/pii/S009286741630424X.

44. Scarborough, E. A., T. N. Davis, and C. L. Asbury, 2019. Tight bending of the Ndc80 complex provides intrinsic regulation of its binding to microtubules. *eLife* 8:e44489. https://elifesciences.org/articles/44489.

45. Roscioli, E., T. E. Germanova, C. A. Smith, P. A. Embacher, M. Erent, A. I. Thompson, N. J. Burroughs, and A. D. McAinsh, 2020. Ensemble-Level Organization of Human Kinetochores and Evidence for Distinct Tension and Attachment Sensors. *Cell Reports* 31:107535. https://linkinghub.elsevier.com/retrieve/pii/S2211124720304356.

46. Sokurenko, E. V., V. Vogel, and W. E. Thomas, 2008. Catch-Bond Mechanism of Force-Enhanced Adhesion: Counterintuitive, Elusive, but . . . Widespread? *Cell Host Microbe* 4:314–323. https://linkinghub.elsevier.com/retrieve/pii/S1931312808003004.

47. Schneider, S. W., S. Nuschele, A. Wixforth, C. Gorzelanny, A. Alexander-Katz, R. R. Netz, and M. F. Schneider, 2007. Shear-induced unfolding triggers adhesion of von Willebrand factor fibers. *Proc. Natl. Acad. Sci.* 104:7899–7903. http://www.pnas.org/cgi/doi/10.1073/pnas.0608422104.

48. Interlandi, G., and W. Thomas, 2010. The catch bond mechanism between von Willebrand factor and platelet surface receptors investigated by molecular dynamics simulations. *Proteins Struct. Funct. Bioinforma.* 78:2506–2522. https://onlinelibrary.wiley.com/doi/10.1002/prot.22759.

49. Arbore, C., M. Sergides, L. Gardini, G. Bianchi, A. Kashchuk, I. Pertici, P. Bianco, F. Pavone, and M. Capitanio, 2021. α-catenin switches between a slip and an asymmetric catch bond with F-actin to cooperatively regulate cell junction fluidity. *bioRxiv* https://www.biorxiv.org/content/early/2021/09/02/2020.04.15.035527.

50. Wimbish, R. T., and J. G. DeLuca, 2020. Hec1/Ndc80 Tail Domain Function at the Kinetochore-Microtubule Interface. *Frontiers in Cell and Developmental Biology* 8:1–16. https://www.frontiersin.org/article/10.3389/fcell.2020.00043/full.

51. Hvidt, S., J. D. Ferry, D. L. Roelke, and M. L. Greaser, 1983. Flexibility of light meromyosin and other coiled-coil α-helical proteins. *Macromolecules* 16:740–745. https://pubs.acs.org/doi/abs/10.1021/ma00239a007.

52. Berg-Sørensen, K., and H. Flyvbjerg, 2004. Power spectrum analysis for optical tweezers. *Review of Scientific Instruments* 75:594–612. http://aip.scitation.org/doi/10.1063/1.1645654.

53. Tolić-Nørrelykke, I. M., K. Berg-Sørensen, and H. Flyvbjerg, 2004. MatLab program for precision calibration of optical tweezers. *Computer Physics Communications* 159:225–240. https://linkinghub.elsevier.com/retrieve/pii/S0010465504001043.

54. Nicholas, M. P., L. Rao, and A. Gennerich, 2014. An Improved Optical Tweezers Assay for Measuring the Force Generation of Single Kinesin Molecules. *In* D. J. Sharp, editor, Methods in Molecular Biology, Springer New York, New York, NY, volume 1136 of *Methods in Molecular Biology*, 171–246. http://dx.doi.org/10.1007/978-1-4939-0329-0_7.

55. Visscher, K., and S. M. Block, 1998. Versatile optical traps with feedback control. *In* Methods in Enzymology, volume 298, 460–489. https://linkinghub.elsevier.com/retrieve/pii/S0076687998980405.

56. Neuman, K. C., and S. M. Block, 2004. Optical trapping. *Review of Scientific Instruments* 75:2787–2809. http://aip.scitation.org/doi/10.1063/1.1785844.

57. Sarshar, M., W. T. Wong, and B. Anvari, 2014. Comparative study of methods to calibrate the stiffness of a single-beam gradient-force optical tweezers over various laser trapping powers. *Journal of Biomedical Optics* 19:115001. http://biomedicaloptics.spiedigitallibrary.org/http://biomedicaloptics.spiedigitallibrary.org/article.aspx?doi=10.1117/1.JBO.19.11.115001.

58. Holland, P. W., and R. E. Welsch, 1977. Robust regression using iteratively reweighted least-squares. *Communications in Statistics - Theory and Methods* 6:813–827. http://www.tandfonline.com/doi/abs/10.1080/03610927708827533.

59. de Menezes, D., D. Prata, A. Secchi, and J. Pinto, 2021. A review on robust M-estimators for regression analysis. *Computers & Chemical Engineering* 147:107254. https://linkinghub.elsevier.com/retrieve/pii/S0098135421000326.

60. Casella, G., and R. L. Berger, 2002. Statistical inference. Duxbury, Pacific Grove, CA 93950 USA, 2 edition.